In-medium nucleon-nucleon cross section in nuclear matter

S. C. Han,[1,2] X. L. Shang,[1,2,*] W. Zuo,[1,2] G. C. Yong,[1,2] and Y. Gao[3]
[1]*CAS Key Laboratory of High Precision Nuclear Spectroscopy, Institute of Modern Physics, Chinese Academy of Sciences, Lanzhou 730000, China*
[2]*School of Nuclear Science and Technology, University of Chinese Academy of Sciences, Beijing 100049, China*
[3]*School of Information Engineering, Hangzhou Dianzi University, Hangzhou 310018, China*

(Received 24 September 2022; accepted 9 December 2022; published 30 December 2022)

In-medium nucleon-nucleon (*NN*) cross sections at various densities and isospin asymmetries are investigated systematically in the framework of the Brueckner-Hartree-Fock approach. The calculations are base on the exact treatment of the center-of-mass momentum instead of the total momentum approximation employed in previous works. The neutron-proton in-medium cross section is shown to exhibit nearly isospin asymmetry independence. For convenience in application, analytical formulas embodying the medium correction to free *NN* cross section with parameters calibrated to the calculated results have been provided. Using these formulas, the transverse and elliptic flows of emitted nucleons in heavy-ion collisions are studied within the isospin-dependent Boltzmann-Uehling-Uhlenbeck transport model. We find the medium effect of the cross section from the *G* matrix contributes to the transverse and elliptic flows oppositely to and obviously smaller than that from the effective mass. In addition, the present microscopic in-medium cross sections can significantly revise the predictions of the transverse and elliptic flows compared to the in-medium cross sections previously adopted in transport models for heavy-ion collisions.

DOI: 10.1103/PhysRevC.106.064332

I. INTRODUCTION

The in-medium nucleon-nucleon (*NN*) cross sections play an essential role in the related topics of neutron stars (NSs) and the transport-model simulation of heavy-ion collisions (HICs) [1–8]. For NSs, the shear viscosity is the primary damping mechanism that hinders the gravitational-wave-driver *r*-mode instability of rapidly rotating NSs at low temperature [9–11], while the thermal conductivity, which measures the ability to conduct the heat, is an important input for modeling NS cooling [12,13]. These two transport coefficients crucially depend on the effective *NN* scattering cross sections near Fermi momentum [7,8]. In the numerical HIC simulations by transport models such as the isospin-dependent Boltzmann-Uehling-Uhlenbeck model [14,15], particles drift in the presence of the mean field while undergoing two-body scatterings, which requires the knowledge of in-medium *NN* cross sections and the nuclear mean field. Microscopic approaches, which can determine both the mean-field and the two-body *NN* cross sections self-consistently based on the bare *NN* force, exhibit the unique advantage of deriving these inputs on the same footing. In the previous literature, several calculations of the effective *NN* cross sections had been performed based on microscopic approaches, such as the Brueckner theory [16,17], the Dirac-Brueckner theory [18–20], variational approaches [21], and so on.

In comparison to the free-space *NN* cross sections, the in-medium effects originate from the scattering amplitude and the density of the states [17]. In the Brueckner theory, the effective *G* matrix, which embodies the many-body effects on *NN* collisions via the mean field and the Pauli blocking, serves as the in-medium scattering amplitude. In the zero density limit, the *G* matrix develops into the *T* matrix, and the corresponding Brueckner-Bethe-Goldstone (BBG) equation reduces to the Lippmann-Schwinger (LS) equation. One can obtain the free-space *NN* cross section directly by solving the LS equation. In addition to the scattering amplitude, the modified density of states due to the many-body effects is essentially determined by nucleon effective masses. These two contributions, i.e., the modification of the *G*-matrix elements, and the modification of the density of states in the medium, can be embodied self-consistently in the Brueckner theory. Actually, the latter in-medium effect strongly overwhelms the first one.

In medium, the cross section depends on the motion state of the colliding pair with respect to the medium, i.e., the momenta of the two colliding nucleons $\mathbf{k}_1$ and $\mathbf{k}_2$. Accordingly, the in-medium *NN* cross section relies on the total momentum of the colliding pair $K = |\mathbf{k}_1 + \mathbf{k}_2|$ besides its dependence on the scattering angle θ and relative momentum $k = \frac{1}{2}|\mathbf{k}_1 - \mathbf{k}_2|$. This K dependence requires an exact treatment of the total momentum of the intermediate two nucleons in solving the BBG equation. However, due to the computational limits, the total momentum was approximated by its average value [22] in previous Brueckner-Hartree-Fock (BHF) calculations [18,23–30]. The current computing power

*shangxinle@impcas.ac.cn

allows one to completely avoid this approximation to obtain more reliable knowledge of the in-medium cross section. Recent studies [31,32] have also shown that an exact treatment of the total momentum can provide more accurate results of the effective mass and the G matrix. On the other hand, in the transport model [33], the medium effect on the cross section is usually approximated by using the effective reduced mass of the scattering pair based on effective NN interactions [34–37]. This approximation is reasonable but not accurate enough. Therefore, we present microscopic predictions of in-medium NN cross sections for asymmetric nuclear matter within the BHF approach under the exact treatment of the total momentum. And we also adopt the obtained cross section to study the medium effect of NN cross sections on some observables in the final state of HICs.

The paper is organized as follows. In the next section, we briefly review the BHF approach and the cross section. The numerical results and discussions are given in Sec. III, where parametrized formulas of the medium correction factor are provided and we employ the obtained formulas to study the medium effect of NN cross sections on heavy-ion reactions. And finally, a summary is given in Sec. IV.

II. THEORETICAL APPROACHES

The calculation of in-medium NN cross sections requires two central ingredients, i.e., the scattering amplitude and the density of states. In the framework of the nonrelativistic BHF approximation, the effective G matrix playing the role of the scattering amplitude and the (momentum dependent) effective mass related to the density of states can be obtained self-consistently.

A. Cross section in the BHF approach

The details of the BHF approach are described elsewhere [23,24,32]. Here we outline it briefly for completeness. The starting point in Brueckner theory is the effective reaction matrix G, which satisfies the generalized Bethe-Goldstone (BG) equation,

$$\begin{aligned}\langle 12|G_{\tau\tau'}(\omega)|1'2'\rangle &= \langle 12|V_{\tau\tau'}|1'2'\rangle + \sum_{1''2''}\langle 12|V_{\tau\tau'}|1''2''\rangle \\ &\times \frac{Q_{\tau\tau'}}{\omega - e_\tau(1'') - e_{\tau'}(2'')}\langle 1''2''|G_{\tau\tau'}(\omega)|1'2'\rangle, \quad (1)\end{aligned}$$

where Q, ω, and $e(\omega)$ are the Pauli operator, the starting energy, and the energy denominator, respectively. V is the adopted Argonne V_{18} NN potential [38] supplemented with an effective two-body force derived from a microscopic three-body force (3BF) [39–41], and $1 \equiv (\mathbf{k}_1, \sigma_1)$, etc., denote the momentum and spin z components. The spin-up and spin-down states are degenerate for non-spin-polarized nuclear matter; hence, we omit the spin index for convenience hereafter. The Pauli operator, defined as

$$Q_{\tau\tau'}(\mathbf{k}_1, \mathbf{k}_2) = [1 - n_\tau(\mathbf{k}_1)][1 - n_{\tau'}(\mathbf{k}_2)], \quad (2)$$

embodies partially many-body effects in the G matrix via preventing the intermediate nucleons from scattering into the occupied states. By $n_\tau(k)$ we denote the Fermi distribution function, which turns into the Heaviside step function $\theta^\tau(k - k_F^\tau)$ at zero temperature. The neutron and proton Fermi momenta are related to their corresponding densities $\rho_{n/p}$ by the relation $k_F^{n/p} = [3\pi^2\rho(1 \pm \beta)/2]^{1/3}$, with the total density $\rho = \rho_n + \rho_p$ and the isospin asymmetry $\beta = (\rho_n - \rho_p)/\rho$.

The single-particle (s.p.) energy in the BHF approach is given by

$$e_\tau(\mathbf{k}) = \frac{\mathbf{k}^2}{2m} + U_\tau(\mathbf{k}), \quad (3)$$

where $U_\tau(\mathbf{k})$ is the so-called *auxiliary* potential, which provides the remaining many-body effects in the G matrix. The choice of $U_\tau(\mathbf{k})$ controls the convergence rate of the hole-line expansion. In the present calculations, the so-called continuous choice of the s.p. potential has been adopted, because it minimizes the contribution from the three-hole line diagrams [42]. Under the continuous choice, the s.p. potential takes the real part of the on-shell antisymmetrized G matrix,

$$U_\tau(\mathbf{k}) = \sum_{\mathbf{k}',\tau'} \mathrm{Re}\langle \mathbf{k}\mathbf{k}'|G_{\tau\tau'}\left[e_{\mathbf{k}}^\tau + e_{\mathbf{k}'}^{\tau'}\right]|\mathbf{k}\mathbf{k}'\rangle_A, \quad (4)$$

for all momenta. In this context, the *auxiliary* potential plays the role of the nuclear mean field that each nucleon feels during its propagation between two successive scatterings.

After several self-consistent iterations of Eqs. (1) and (3), the effective interaction matrix G is obtained for the given density and isospin asymmetry. Using the G matrix, the total NN elastic-scattering cross section in asymmetric nuclear matter can be expressed as

$$\sigma = \frac{M^{*2}}{16\pi^2\hbar^4}\sum_{S,J}\sum_{L',L}[1 - (-1)^{S+L+T}]^2\frac{2J+1}{4\pi}\left|G_{L'L}^{SJ}\right|^2, \quad (5)$$

where $G_{L'L}^{SJ} = \langle k, L'SJ|G(e_2)|k, LSJ\rangle$ is the matrix element of the on-shell G matrix in the the partial wave representation, with T, S, L, and J denoting the total isospin, the total spin, the orbital angular momentum, and the total angular momentum of the two scattering nucleons, respectively. $e_2 = e_{\mathbf{k}_1}^\tau + e_{\mathbf{k}_2}^{\tau'}$ denotes the total energy of the colliding pair. And the term $1 - (-1)^{S+L+T}$ originates from the generalized Pauli principle. M^*, describing the in-medium phase-space modification, represents the effective mass of the two-nucleon system in medium [17,43]. It is determined by the dependence of the total energy of the pair e_2 on the relative $k = |\mathbf{k}_1 - \mathbf{k}_2|/2$ and is defined as

$$M^* = \left(\frac{1}{2k}\frac{\partial e_2}{dk}\right)^{-1}. \quad (6)$$

This definition coincidentally develops into the reduced effective mass of two particles in the case when the momenta of the colliding particles are equal or the s.p. potential is parabolic. In some investigations, the reduced effective mass is employed for simplicity [7,27]. However, in the present

calculation we adopt the definition (6) to include the total momentum contribution accurately (see Sec. II C).

B. Three-body force

Our adopted 3BF is constructed within the meson-exchange-current approach, and one can refer to Refs. [39–41] for all lengthy technical details. In this model, the most important mesons (π, ρ, σ, and ω) are considered, and the Δ and Roper resonance excitations and the important Z diagram are involved. All parameters of the TBF model, i.e., the coupling constants and form factors, are consistently determined to reproduce the Argonne V_{18} NN potential, and their values can be found in Refs. [40,41]. After integrating over the degrees of freedom of the third nucleon, an equivalent effective two-body force, $V_3^{\rm eff}$, can be obtained from the microscopic 3BF according to the standard scheme as described in Ref. [39]. In r space, the effective two-body force $V_3^{\rm eff}$ reads

$$\begin{aligned}\langle \mathbf{r}_1', \mathbf{r}_2'|V_3^{\rm eff}|\mathbf{r}_1, \mathbf{r}_2\rangle &= \frac{1}{4}{\rm Tr}\sum_n \int d\mathbf{r}_3' d\mathbf{r}_3 \phi_n^*(\mathbf{r}_3')[1-\eta(r_{13}')][1-\eta(r_{23}')] \\ &\times W_3(\mathbf{r}_1', \mathbf{r}_2', \mathbf{r}_3'|\mathbf{r}_1, \mathbf{r}_2, \mathbf{r}_3)\phi_n(\mathbf{r}_3) \\ &\times [1-\eta(r_{13})][1-\eta(r_{23})], \end{aligned} \tag{7}$$

where ϕ_n is the wave function of a single nucleon in free space and the trace is taken with respect to the spin and isospin of the third nucleon. The details of the 3BF $W_3(\mathbf{r}_1', \mathbf{r}_2', \mathbf{r}_3'|\mathbf{r}_1, \mathbf{r}_2, \mathbf{r}_3)$ are described in Ref. [40]. The defect function $\eta(r)$ is determined by the G matrix, which should be calculated self-consistently with the BG equation. We stress here that the defect function implicitly depends on the value of the total momentum and the total momentum approximation is abandoned to determine the defect function in the present calculation. One should note that the current effective 3BF, avoiding the difficult problem to solve the Faddeev equation, neglects certain many-body contributions [44,45].

C. Total-momentum-dependent G matrix

Both the G matrix and the effective mass depend on the motion states of the colliding pairs with respect to the medium or, equivalently, the in-medium cross sections depend on the total momentum of the colliding pair. Using the definitions of total and relative momenta,

$$\mathbf{K} = \mathbf{k}_1 + \mathbf{k}_2, \quad \mathbf{k} = \tfrac{1}{2}(\mathbf{k}_1 - \mathbf{k}_2), \tag{8}$$

the BG equation (1) develops into

$$\begin{aligned}\delta_{\mathbf{K}\mathbf{K}'}\langle \mathbf{k}|G_{\tau\tau'}(\mathbf{K},\omega)|\mathbf{k}'\rangle &= \delta_{\mathbf{K}\mathbf{K}'}\langle \mathbf{k}|V_{\tau\tau'}|\mathbf{k}'\rangle + \sum_{\mathbf{K}''\mathbf{k}''}\delta_{\mathbf{K}\mathbf{K}''}\langle \mathbf{k}|V_{\tau\tau'}|\mathbf{k}''\rangle \\ &\times \frac{Q_{\tau\tau'}(\mathbf{K}'',\mathbf{k}'')}{\omega - e_\tau\left(\frac{1}{2}\mathbf{K}''+\mathbf{k}''\right) - e_{\tau'}\left(\frac{1}{2}\mathbf{K}''-\mathbf{k}''\right)} \\ &\times \delta_{\mathbf{K}''\mathbf{K}'}\langle \mathbf{k}''|G_{\tau\tau'}(\mathbf{K}'',\omega)|\mathbf{k}'\rangle. \end{aligned} \tag{9}$$

The conservation condition of total momentum during scattering ensures $\mathbf{K} = \mathbf{K}' = \mathbf{K}''$. Though the bare NN interaction V is independent of the total momentum, the G matrix depends on $\mathbf{K}$ due to the Pauli operator and the energy denominator in the BG equation. For given densities and isospin asymmetries, the calculations of the *auxiliary* potential (4) require the full information of G at arbitrary values of ω and $K = |\mathbf{K}|$ (note the G matrix should be independent of the orientation of $\mathbf{K}$). Therefore, one needs to solve the BG equation (9) on a $N_K \times N_\omega$ grid, where $N_K(N_\omega)$ is the number of $K(\omega)$ points. It would have been greatly challenging to do such calculation several decades ago. Accordingly, the total momentum has been approximated by its averaged value [22],

$$\begin{aligned}\langle K_{\tau\tau'}^2\rangle(k) &= \frac{\int d\mathbf{k}_1 \int d\mathbf{k}_2 n^\tau(k_1) n^{\tau'}(k_2)\mathbf{K}^2\delta(k-|\mathbf{k}_1-\mathbf{k}_2|/2)}{\int d\mathbf{k}_1 \int d\mathbf{k}_2 n^\tau(k_1) n^{\tau'}(k_2)\delta(k-|\mathbf{k}_1-\mathbf{k}_2|/2)}. \end{aligned} \tag{10}$$

Reference [32] indicates that this approximation is insufficient to obtain accurate results. In the present calculation, the exact treatment of the total momentum is employed in the calculation of the G matrix and the s.p. potential.

To obtain the in-medium cross section, the on-shell condition of the scattering amplitude requires the starting energy in the G matrix to be $\omega = e_2$, where e_2 is actually a very complicated function of the total momentum K, the relative momentum k, and the angle $\theta_{\widehat{\mathbf{K}\mathbf{k}}}$ between $\mathbf{K}$ and $\mathbf{k}$. Fortunately, the total energy e_2 is insensitive to the angle $\theta_{\widehat{\mathbf{K}\mathbf{k}}}$. In addition, one may note that the total energy of the pair in the intermediate state, i.e., $e_\tau(\frac{1}{2}\mathbf{K}''+\mathbf{k}'') + e_{\tau'}(\frac{1}{2}\mathbf{K}''-\mathbf{k}'')$ in the energy denominator of Eq. (9), is angle-averaged in solving the BG equation (9) to get the G matrix. It has been shown in Ref. [32] that such an angle-average procedure provides a fairly accurate approximation. To be consistent, it seems more appropriate to take the average of e_2 with respect to the angle $\theta_{\widehat{\mathbf{K}\mathbf{k}}}$ in M^* and $G_{L'L}^{SJ} = \langle k, L'SJ|G(e_2)|k, LSJ\rangle$ of Eq. (5) for calculating the cross sections; i.e., the total energy e_2 is approximated by its angle-averaged value, i.e., $e_2 \to \overline{e_2} = \int \frac{d\Omega_{\mathbf{k}}}{4\pi} e_2$, in the present calculation. In fact, this angle-averaged approximation is also adopted in dealing with the Pauli operator in solving the BG equation, which can eliminate the coupling between different partial waves and the mixing of total isospin $T = 1$ and $T = 0$ neutron-proton states in the G matrix [32]. After the angle-averaging procedure, both the G matrix and the effective mass of the two-nucleon system M^* depend simply on the magnitudes K and k of the total momentum and the relative momentum, while k is essentially related to the laboratory energy through the relation $E_{\rm Lab} = 2\frac{\hbar^2 k^2}{m}$. Finally, the in-medium cross section is essentially a function of the density ρ, the isospin asymmetry β, the total momentum K of the colliding pair, and the incident laboratory energy $E_{\rm Lab}$.

III. RESULTS AND DISCUSSION

In this section, we first obtain the parametric formulas of the in-medium cross sections based on the microscopic calculations. Following that, we apply the obtained formulas to the isospin-dependent Boltzmann-Uehling-Uhlenbeck

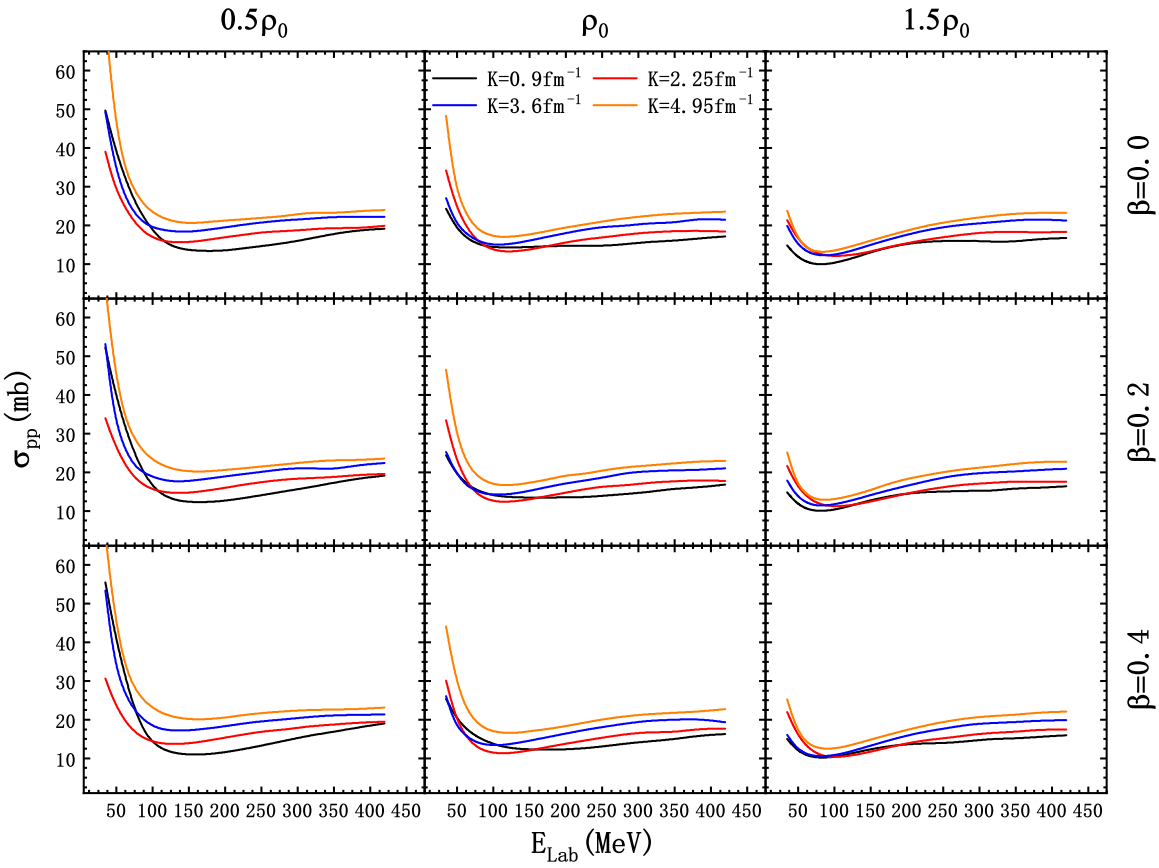

FIG. 1. The calculated pp cross sections within the BHF approach as a function of the incident laboratory energy $E_{\rm Lab}$. The left, middle, and right panels correspond to the densities $0.5\rho_0$, ρ_0, and $1.5\rho_0$, respectively. While the upper, middle, and lower panels show the results with various isospin asymmetries $\beta = 0.0$, 0.2, 0.4. The black, red, blue, and orange lines correspond to the total momenta 0.9, 2.25, 3.6, and 4.95 fm^{-1}, respectively.

(IBUU) transport model [33] to study medium effects of the cross sections on the transverse and elliptic flows in HICs.

A. In-medium NN cross section

The numerical calculation here focuses on obtaining extensive information of the in-medium NN cross sections under various densities and isospin asymmetries based on the BHF approach at zero temperature. The Argonne V_{18} two-body interaction [38] supplemented with a microscopic 3BF [40,41] is adopted as the realistic NN interaction.

In comparison to the free-space NN cross sections, which rely only on the incident laboratory energy $E_{\rm Lab}$, the in-medium cross sections also depend on the density ρ, the isospin asymmetry β, and the total momentum K, due to the medium effect. To exhibit these dependencies, the in-medium proton-proton (pp), neutron-neutron (nn), and neutron-proton (np) cross sections are shown in Figs. 1–3 as functions of $E_{\rm Lab}$ at various densities ρ and isospin asymmetries β with different total momenta K, respectively. To exhibit the effect of the total momentum, the in-medium cross sections with different total momenta, $K = 0.9$, 2.25, 3.6, and 4.95 fm^{-1}, are displayed. The left, middle, and right panels correspond to densities $0.5\rho_0$, ρ_0, and $1.5\rho_0$, with the saturation density $\rho_0 = 0.17$ fm^{-3}, respectively. The upper, middle, and lower panels show the results with several values of isospin asymmetry, $\beta = 0.0$, 0.2, and 0.4.

In Figs. 1 and 2, the pp and nn cross sections do not vary monotonically with the incident laboratory energy; i.e., the cross sections decrease rapidly at low $E_{\rm Lab}$, while they come to increase slowly at high $E_{\rm Lab}$. This is in agreement with the conclusions of Refs. [7,27]. Such a behavior at high $E_{\rm Lab}$ of the cross section originates from the 3BF effect [8]. However, the np cross section decreases monotonically with $E_{\rm Lab}$. In general, the effective mass decreases with density below 3 times saturation density [31]. Because the medium effect from the effective mass strongly overwhelms that from the G matrix on the cross sections [17], the cross sections decrease with densities at low incident energy as exhibited in Figs. 1–3. In addition, the nn cross section is systematically greater than the corresponding pp one, which can be attributed to the mass-splitting feature of $m_n^* > m_p^*$ in the BHF approach.

On the whole, the in-medium cross section grows with increasing total momentum at high $E_{\rm Lab}$. The situation turns to be a little complicated for low $E_{\rm Lab}$. As is well known, the G matrix shows a spurious singular behavior around Fermi

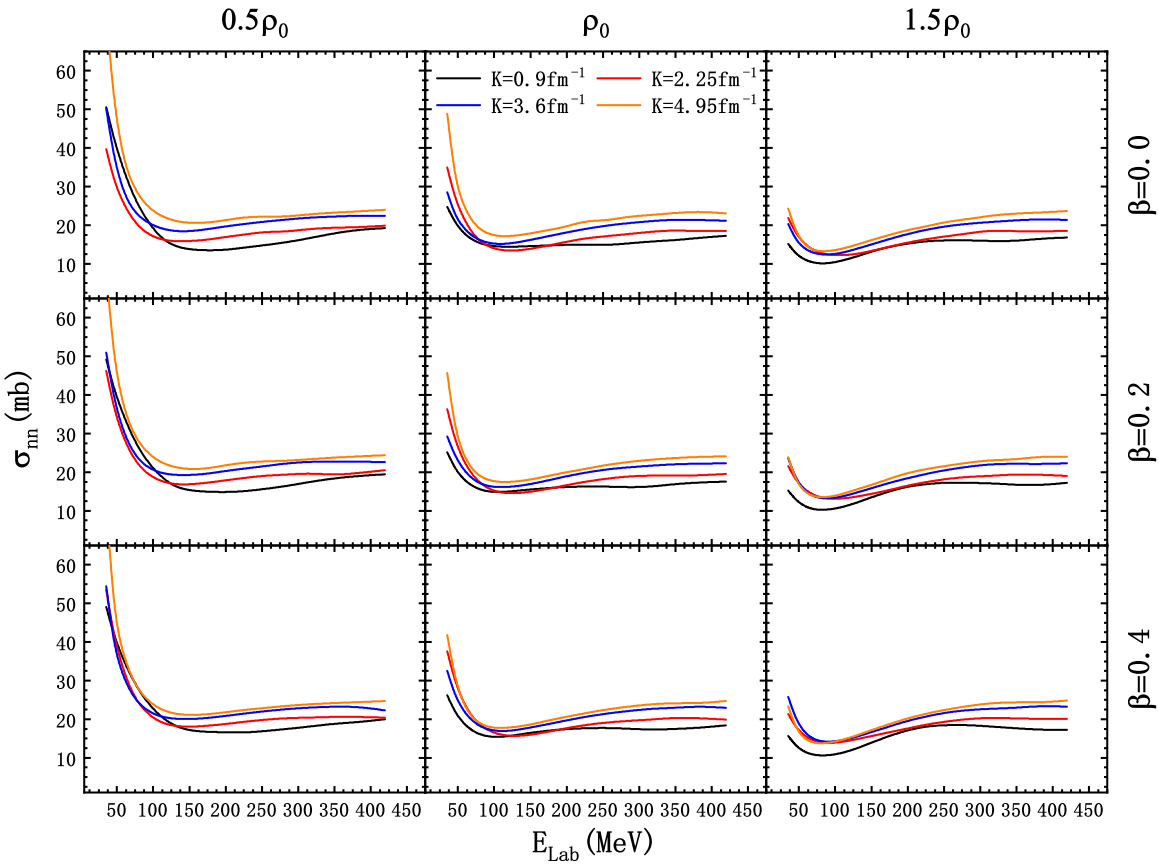

FIG. 2. Same as in Fig. 1, but for *nn* cross sections.

energy corresponding to the missing pair correlation from the BHF approximation [46–50]. This singularity occurs when the total momentum is close to zero and strongly enhances the cross section in a sharp region near the Fermi surface [17,27], which makes an empirical parametrization of the cross section rather difficult. However, in heavy-ion collisions, this strong enhancement has nonsignificant influence on the numerical simulation. Accordingly, we eliminate the singularity by hand when obtaining the parametrized formulas. As soon as the total momentum becomes nonzero, the abovementioned enhancement in the cross section disappears rapidly, which results in the complicated behavior for different K at low incident energy.

One can see from Fig. 3 that there are only tiny discrepancies among the *np* cross sections at various isospin asymmetries. In fact, the medium correction factor based on the reduced mass of two colliding nucleons implies a significantly weak isospin asymmetry dependence [34–36]. Because the effect from the effective mass dominates the medium effects of the cross section, the result remains faint isospin asymmetry dependence when the effect from the G matrix is included. Such an isospin-asymmetry-independent in-medium cross section is also employed in the ultrarelativistic quantum molecular dynamics (UrQMD) model [51–53] to simulate HICs. In the following parametrization of the *np* in-medium cross section, we adopt the isospin asymmetry independence.

Because the free *pp* and *np* cross sections can be determined experimentally [54–56], in some numerical simulation of HICs using BUU [34–36,51–53] and QMD transport models, the in-medium cross sections are factorized as the product of medium correction factors and the free *NN* elastic-scattering cross sections σ_{free}. In such a factorization, the medium effects are involved in the medium correction factor evidently. Especially, if one approximates the medium effect to the phase-space modification, the medium effect can be simply expressed as the square of the ratio of the effective reduced mass to the bare reduced mass of the two colliding nucleons [34]. To better connect with the transport model, we parametrize the medium correction factor, which is defined as

$$\lambda = \sigma_{\text{BHF}}/\sigma_{\text{free}}, \tag{11}$$

where σ_{BHF} represents the calculated in-medium cross section in the framework of the BHF approach.

One of the main goals of the current paper is to provide an easy-to-use microscopic nuclear input for HIC simulations. We, therefore, fit the obtained medium correction factors as analytic functions of four independent variables including the density $\widetilde{\rho} = \rho/\rho_0$, the isospin asymmetry β, the total momentum K, and the incident laboratory energy $\widetilde{E}_{\text{Lab}} = E_{\text{Lab}}/419.58$ MeV. The empirical formulas for the *pp* and *nn* medium correction factors are employed as

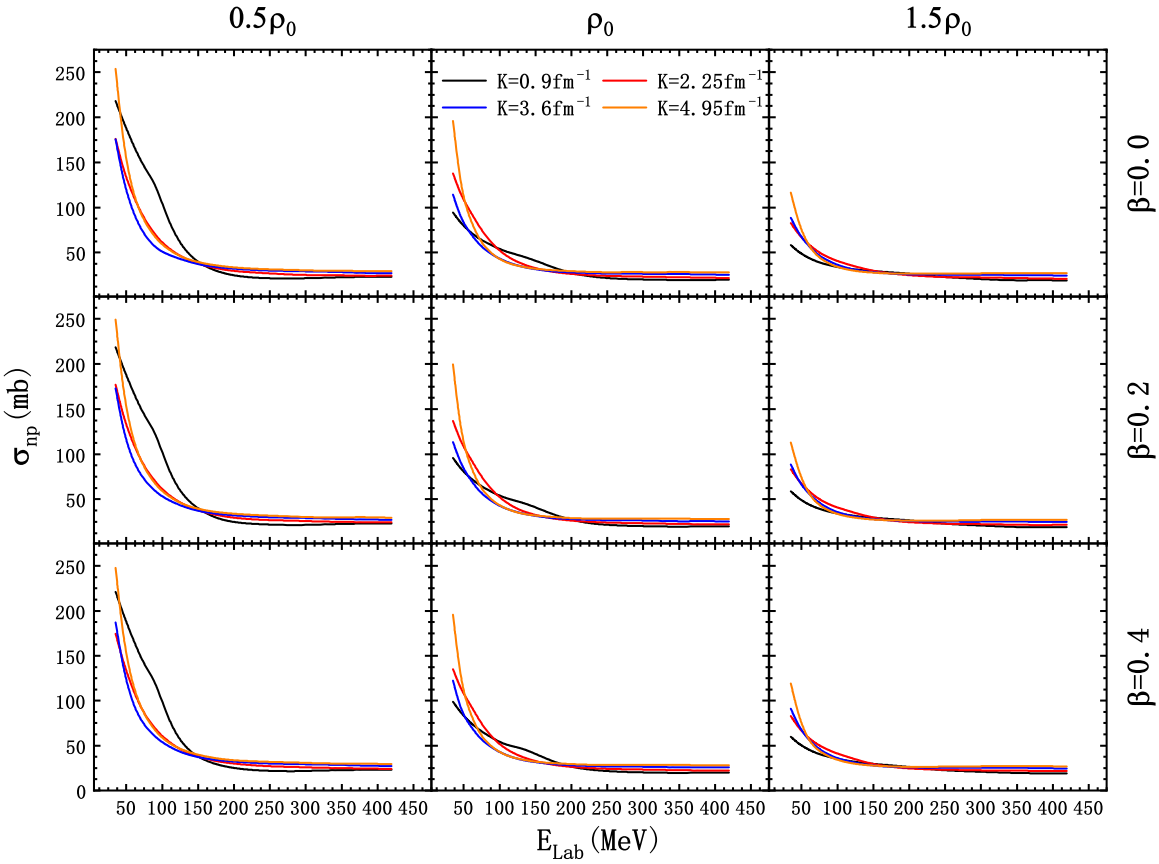

FIG. 3. Same as in Fig. 1, but for *np* cross sections.

follows:

$$\begin{aligned}\lambda_{pp} = &\{1+[(a_1+a_2\widetilde{\rho}K^{0.5}+a_3K^2+a_4\widetilde{\rho}^2+a_5\widetilde{E}_{\rm Lab}K+a_6\widetilde{E}_{\rm Lab}^{0.5}+a_7\widetilde{E}_{\rm Lab}^2)\widetilde{\rho}^{0.5}\\ &+(a_8\widetilde{\rho}^{0.5}+a_9\widetilde{\rho}+a_{10}\widetilde{\rho}^2+a_{11}\widetilde{\rho}^{1.5}\widetilde{E}_{\rm Lab}+a_{12}\widetilde{\rho}^2\widetilde{E}_{\rm Lab}^3)\beta]/[1+(a_{13}+a_{14}\widetilde{\rho}^{1.5}+a_{15}K^2)\widetilde{E}_{\rm Lab}+a_{16}\widetilde{E}_{\rm Lab}^2+a_{17}\widetilde{E}_{\rm Lab}^3]\}\\ &\times\{1+[a_{18}\widetilde{\rho}^{0.5}+a_{19}\widetilde{\rho}K^2+a_{20}\widetilde{\rho}^{0.5}K^3+a_{21}\widetilde{\rho}^2K^{0.7}]/[1+(a_{22}+a_{23}\widetilde{\rho}^{0.5}+a_{24}K^2)\widetilde{E}_{\rm Lab}+a_{25}\widetilde{E}_{\rm Lab}^2]\},\end{aligned} \tag{12}$$

$$\begin{aligned}\lambda_{nn} = &\{1+[(a_1+(a_2\widetilde{\rho}+a_3)K^{1.5}+a_4\widetilde{\rho}^2+a_5\widetilde{E}_{\rm Lab}K^{0.5}+a_6\widetilde{E}_{\rm Lab}^{0.5}+a_7\widetilde{E}_{\rm Lab}^2)\widetilde{\rho}^{0.5}\\ &+(a_8\widetilde{\rho}^{0.5}+a_9\widetilde{\rho}+a_{10}\widetilde{\rho}^2+a_{11}\widetilde{\rho}^{1.5}\widetilde{E}_{\rm Lab}+a_{12}\widetilde{\rho}^2\widetilde{E}_{\rm Lab}^3)\beta]/[1+(a_{13}+a_{14}\widetilde{\rho}^{1.5}+a_{15}K^2)\widetilde{E}_{\rm Lab}+a_{16}\widetilde{E}_{\rm Lab}^2+a_{17}\widetilde{E}_{\rm Lab}^3]\}\\ &\times\{1+[a_{18}\widetilde{\rho}^{1.5}\widetilde{E}_{\rm Lab}^2+a_{19}\widetilde{\rho}K^2+a_{20}\widetilde{\rho}^{1.5}K^3+a_{21}\widetilde{\rho}^2K^{0.7}]/[1+(a_{22}+a_{23}\widetilde{\rho}^{0.5}+a_{24}K^2)\widetilde{E}_{\rm Lab}+a_{25}\widetilde{E}_{\rm Lab}^3]\}.\end{aligned} \tag{13}$$

They can both be divided into two parts roughly, one corresponds to the β-dependent part, while the other is related to K dependence. Both of these two terms are ρ and $E_{\rm Lab}$ dependent. Though the exact physical picture of the formulas is unclear, they can provide us with a relatively good fitting of the results. Due to the independence of β, the formula for the *np* medium correction factor is chosen as

$$\begin{aligned}\lambda_{np} = &\{1+[(a_1+a_2\widetilde{\rho}^{0.5}+a_3\widetilde{\rho}^2+a_4\widetilde{E}_{\rm Lab}^{1.5}+a_5\widetilde{E}_{\rm Lab}+a_6\widetilde{E}_{\rm Lab}^3)\widetilde{\rho}^{0.7}]\\ &/[0.01+(a_7+a_8\widetilde{\rho}^2+a_9(0.1K)^2)\widetilde{E}_{\rm Lab}+a_{10}\widetilde{E}_{\rm Lab}^2+a_{11}\widetilde{E}_{\rm Lab}^3]\}\\ &\times\{1+[(a_{12}\widetilde{E}_{\rm Lab}^{0.5}+a_{13}(0.1K)\widetilde{E}_{\rm Lab}^2+a_{14}(0.1K)^{1.5}\widetilde{E}_{\rm Lab}+a_{15}(0.1K)^{0.5})\widetilde{\rho}^{0.7}]\\ &/[0.01+(a_{16}+a_{17}\widetilde{\rho}^{0.5}+a_{18}K^2)\widetilde{E}_{\rm Lab}^{0.5}+a_{19}\widetilde{E}_{\rm Lab}^2]\},\end{aligned} \tag{14}$$

where the term related to β is absent. In the present fitting procedure, the microscopic calculations cover the domains $0.5\rho_0 \leqslant \rho \leqslant 2.5\rho_0$, $-0.8 \leqslant \beta \leqslant 0.8$, $0\ {\rm fm}^{-1} \leqslant K \leqslant 6.3\ {\rm fm}^{-1}$, and $35\ {\rm MeV} \leqslant E_{\rm Lab} \leqslant 420\ {\rm MeV}$. As discussed before, the in-medium cross section is strongly enhanced near the Fermi surface due to the singularity of

TABLE I. Parameters for the formula of the medium correction factors λ_{pp}, λ_{nn}, and λ_{np}.

Type	a_1	a_2	a_3	a_4	a_5	a_6	a_7	a_8	a_9	a_{10}	a_{11}	a_{12}	
	a_{14}	a_{15}	a_{16}	a_{17}	a_{18}	a_{19}	a_{20}	a_{21}	a_{22}	a_{23}	a_{24}	a_{25}	a_{13}
pp	0.3060	−0.0596	0.0119	0.0666	0.0896	−0.482	−0.2739	−0.3801	0.37	−0.1005	−0.059	−0.0404	−4.977
	0.5798	0.0532	8.2144	−2.7922	−0.6403	−0.0049	0.0008	0.0115	−2.8884	1.3864	−0.0042	5.6319	
nn	−0.7353	−0.0096	0.0277	0.013	0.0252	0.219	−0.0036	0.5708	−0.5345	0.0401	0.2511	−0.1032	−0.66
	0.0421	0.0538	1.8716	−1.0733	0.9442	−0.0101	−0.0001	0.0164	−3.4316	0.4414	0.0688	11.0018	
np	−0.0696	−0.07338	0.01371	1.3843	−0.5427	0.0416	−0.2427	−0.6689	−7.4114	1.6452	−3.2383	0.4973	−2.7614
	2.1123	−0.0099	0.1975	−0.7046	−0.0228	−3.4225							

the G matrix when K is close to zero; we artificially remove this singularity. However, the medium correction factors still behave in a complicated way at low total momenta. Such a complexity increases the difficulty of parametrization and may only slightly affect HIC simulation. Accordingly, the cross section near the Fermi surface has been replaced by the interpolated value in order to avoid the complexity at low K ($\leqslant 0.9$ fm^{-1}) during the parametrization procedure in the current paper. Finally, the parameters of the fittings are listed in Table I for *pp*, *nn*, and *np*, respectively.

In Fig. 4, comparisons between the medium correction factors from the formulas (lines with symbols) and from the BHF approach (lines) are displayed. The left, middle, and right panels correspond to densities $0.5\rho_0$, ρ_0, and $1.5\rho_0$, with $\beta = 0.0$, respectively. The upper, middle, and lower panels represent the *pp*, *nn*, and *np* medium correction factors, respectively. Four different medium correction factors with total momenta 0.9, 2.25, 3.6, and 4.95 fm^{-1} are marked with black, red, blue, and orange, respectively. Figure 5 shows the same results as Fig. 4, but for $\beta = 0.2$. Because the *np* in-medium cross section is nearly isospin asymmetry independent, the *np* medium correction factors are not exhibited for $\beta = 0.2$ in Fig. 5. In addition, the free *NN* cross section is identical for different ρ and β; however, this property is broken down

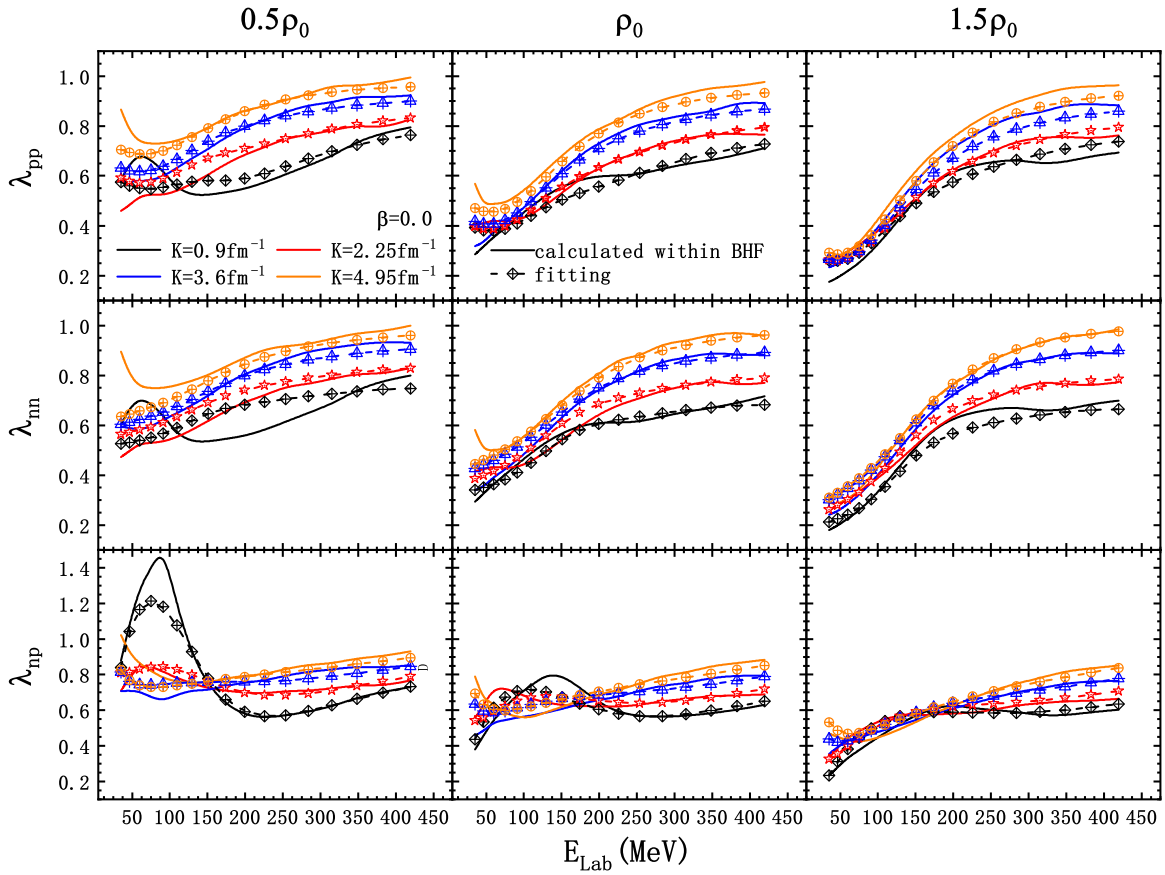

FIG. 4. The medium correction factors as a function of the incident laboratory energy $E_{\rm Lab}$. The upper, middle, and lower panels correspond to *pp*, *nn*, and *np*, respectively. The left, middle, and right panels correspond to densities $0.5\rho_0$, ρ_0, and $1.5\rho_0$, with $\beta = 0.0$, respectively. The black, red, blue, and orange colors correspond to the total momenta 0.9, 2.25, 3.6, and 4.95 fm^{-1}, respectively. The lines are related to the microscopic calculation, while the lines with symbols correspond to the fitting results.

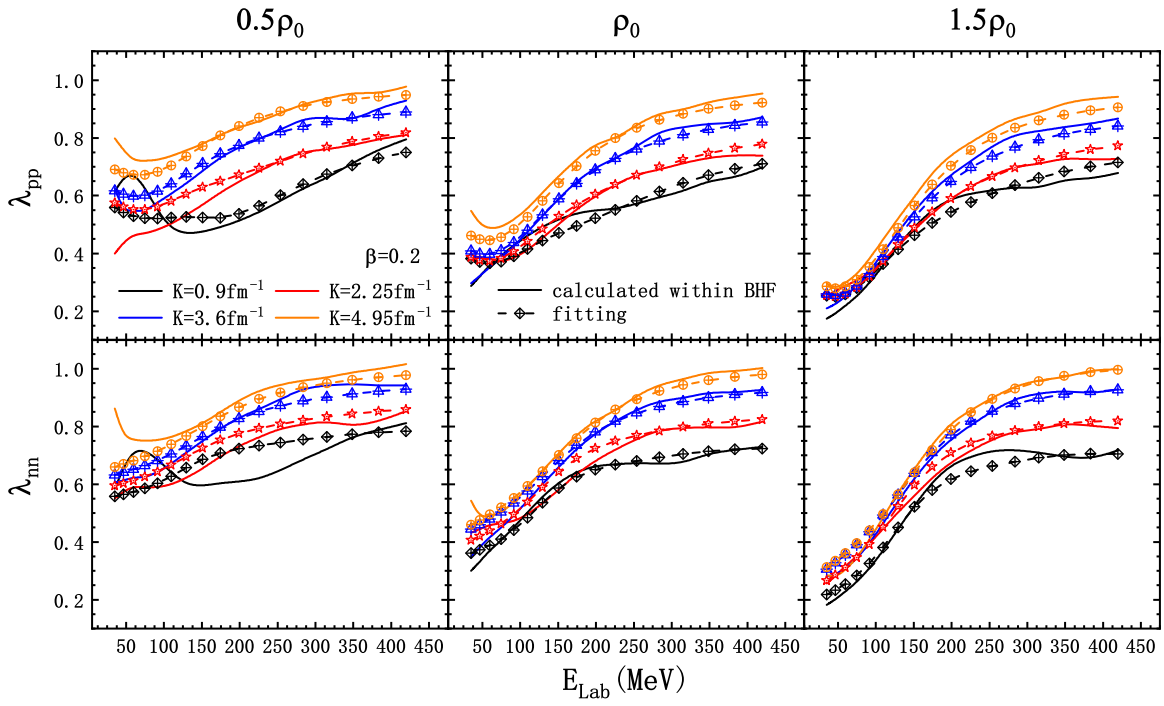

FIG. 5. Same parameters as Fig. 4 except the isospin asymmetry $\beta = 0.2$ and the absence of np.

by the medium correction. The fitting results coincide with the microscopic calculation well except for some complicated cases. The standard deviations for pp, nn, and np are 0.047, 0.0412, and 0.05, respectively. This accuracy might be sufficient for the numerical simulation of HICs as is shown in Sec. III B.

B. Transverse and elliptic flows

One can easily apply the medium correct factors (12), (13), and (14) of cross sections to the IBUU transport model. It was shown in Refs. [35,36,57] that the transverse $\langle p_x \rangle$ and elliptic flows V_2 of emitted nucleons in HICs are sensitive to the NN cross sections. Especially, Ref. [35] indicated that one can extract the many-body effect via the transverse flow without being much affected by the uncertainty of nuclear symmetry energy. Accordingly, we take advantage of the transverse and elliptic flows of emitted nucleons in HICs to study the medium effects of NN elastic-scattering cross sections in the framework of the IBUU transport model. The elliptic flow V_2 is the second Fourier coefficient of the nucleon azimuthal distribution, i.e.,

$$V_2 = \langle \cos(2\phi) \rangle = \left\langle \frac{p_x^2 - p_y^2}{p_t^2} \right\rangle, \tag{15}$$

with the transverse momentum of emitted nucleons,

$$p_t = \sqrt{p_x^2 + p_y^2}. \tag{16}$$

Figure 6 shows the transverse and elliptic flows in semicentral $^{132}\mathrm{Sn} + ^{124}\mathrm{Sn}$ collisions at $E/A = 270$ MeV, respectively. For comparison, five kinds of NN cross sections are adopted, including the free one, σ_{free}; the effective one employed in the previous IBUU model [37], $\sigma_{\mathrm{eff}} = \mu^{*2}\sigma_{\mathrm{free}}$; the microscopic one based on the BHF approach, σ_{BHF}; the one calculated by replacing M^* with vacuum mass in Eq. (5), σ^*_{BHF}; and that obtained from the formulas (12), (13) and (14) σ_{fit}, where μ^* is the effective reduced mass of the scattering nucleons.

Due to the Coulomb repulsion between protons, the transverse and elliptic flows of protons are larger than those of neutrons as exhibited in Fig. 6. The discrepancies among the elliptic flows obtained from different cross sections become larger at higher transverse momenta. This is due to the fact that nucleons emitted with higher transverse momenta undergo more violent collisions, and thus the influence of NN cross sections becomes more important. In addition, Fig. 6 shows that the results obtained from σ_{fit} coincide with those from σ_{BHF}, which indicates the parametrization (12), (13), and (14) can reproduce the in-medium cross section well. The present formulas for nn, pp, and np medium correction factors are sufficiently accurate for the numerical simulation of HICs. Moreover, the discrepancy between the results from σ_{BHF} and from σ_{free} is much larger than that between the results from σ^*_{BHF} and from σ_{free}, which confirms that the medium effect from the effective mass strongly overwhelms that from the G matrix [17]. Furthermore, the medium effect of the cross section from the G matrix provides an opposite contribution to the transverse and elliptic flows compared with the medium effect from the effective mass. One may note that the results obtained from σ_{eff} are between those from σ_{free} and σ_{BHF}. Though the results from σ_{eff} have embodied the medium effect from the effective mass, the calculation of the effective mass is approximated by the effective reduced mass at the Fermi surface. Hence, this approximation is insufficient. The microscopic NN cross sections can lead to significantly different predictions of the transverse and elliptic flows in HICs.

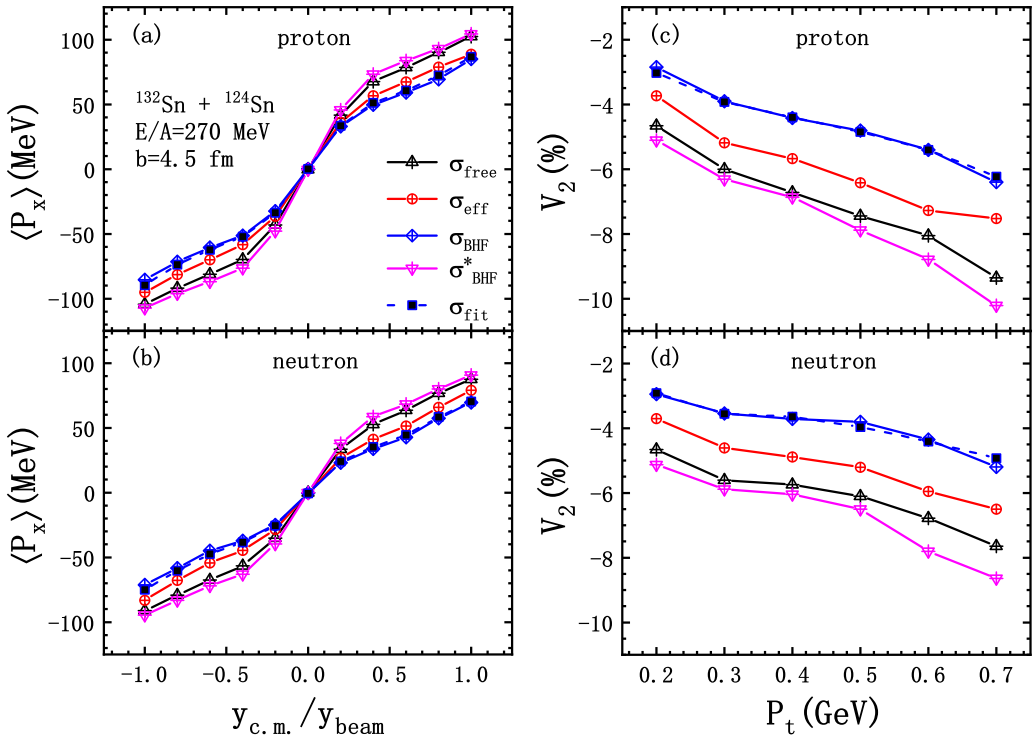

FIG. 6. Proton [panels (a) and (c)] and neutron [panels (b) and (d)] transverse (left panels) and elliptic (right panels) flows in the semicentral reaction of ^{132}Sn + ^{124}Sn at 270 MeV/nucleon. Left panels: Proton (a) and neutron (b) transverse flows as a function of rapidity in the semicentral reaction of ^{132}Sn + ^{124}Sn at 270 MeV/nucleon. Right panels: Proton (c) and neutron (d) elliptic flows as a function of the transverse momentum.

IV. SUMMARY

In conclusion, the in-medium *NN* cross sections have been systematically calculated at various densities and isospin asymmetries for nuclear matter in the framework of the BHF approach with a microscopic 3BF. The total momentum contributions to the medium effect are included to obtain reliable results. We find the *np* in-medium cross section is nearly isospin asymmetry independent. In addition, easy-to-use formulas of the medium correction factors, which can be applied to the transport model conveniently, are provided with the parameters calibrated to the calculated results.

Following this, the obtained *NN* cross sections are employed in the IBUU model to study the medium effect of the cross section on the transverse and elliptic flows in HICs. The results show that the medium effect of the cross section from the *G* matrix contributes to the transverse and elliptic flows oppositely to and obviously smaller than that from the effective mass. Moreover, the previous adopted effective *NN* cross section in the IBUU transport model which embodies the medium effects by the effective reduced mass at the Fermi surface (an approximate consideration of the effective mass of the two scattering nucleons) might be insufficient for studying some observables compared to the current calculated *NN* cross section. Furthermore, the present results also show that our parametrized formulas can reproduce the calculated in-medium *NN* cross section well. Therefore, these analytic formulas can be used to study the medium effect of the cross section on other observables in HICs, which we will explore in a future work.

As is known, the BHF calculation is only appropriately performed for homogeneous and equilibrate matter. The application of the obtained cross sections should be under these restrictions as well. In the standard numerical simulations of HICs using transport models, the phase space of the colliding system is divided into small cells, and the local density approximation is adopted by assuming the matter inside each cell is homogeneous. Under this approximation, the cross sections obtained from the BHF approach can be applied. However, the physical conditions in HICs may be quite different. And consequently, the local density assumption might need to be estimated and one may also need to be careful of the effect due to the deviation from the equilibrium state in HICs.

ACKNOWLEDGMENTS

The work is supported by the National Natural Science Foundation of China (Grants No. 11975282, No. 11505241, No. 11875013, and No. 11435014), the Strategic Priority Research Program of Chinese Academy of Sciences (Grant No. XDB34000000), and the Youth Innovation Promotion Association of Chinese Academy of Sciences (Grant No. Y2021414), the Scientific Research Program Funded by Hangzhou Dianzi University Information Engineering College (No. KYP0222007).

[1] G. D. Westfall *et al.*, Phys. Rev. Lett. **71**, 1986 (1993).
[2] S. Soff, S. A. Bass, C. Hartnack, H. Stöcker, and W. Greiner, Phys. Rev. C **51**, 3320 (1995).
[3] T. Alm, G. Röpke, W. Bauer, F. Daffin, and M. Schmidt, Nucl. Phys. A **587**, 815 (1995).
[4] A. Insolia, U. Lombardo, N. G. Sandulescu, and A. Bonasera, Phys. Lett. B **334**, 12 (1994).
[5] V. de la Mota, F. Sebille, M. Farine, B. Remaud, and P. Schuck, Phys. Rev. C **46**, 677 (1992).
[6] H. F. Zhang, U. Lombardo, and W. Zuo, Phys. Rev. C **82**, 015805 (2010).
[7] P. S. Shternin, M. Baldo, and P. Haensel, Phys. Rev. C **88**, 065803 (2013).
[8] X.-L. Shang, P. Wang, W. Zuo, and J.-M. Dong, Phys. Lett. B **811**, 135963 (2020).
[9] E. Flowers and N. Itoh, Astrophys. J. **230**, 847 (1979).
[10] C. Cutler and L. Lindblom, Astrophys. J. **314**, 234 (1987).
[11] I. Vidaña, Phys. Rev. C **85**, 045808 (2012).
[12] D. Page, U. Geppert, and F. Weber, Nucl. Phys. A **777**, 497 (2006).
[13] D. G. Yakovlev and C. J. Pethick, Annu. Rev. Astron. Astrophys. **42**, 169 (2004).
[14] B. A. Li, Phys. Rev. Lett. **85**, 4221 (2000).
[15] B. A. Li, G. C. Yong, and W. Zuo, Phys. Rev. C **71**, 014608 (2005).
[16] A. Bohnet, N. Ohtsuka, J. Aichelin, R. Linden, and A. Faessler, Nucl. Phys. A **494**, 349 (1989).
[17] H.-J. Schulze, A. Schnell, G. Röpke, and U. Lombardo, Phys. Rev. C **55**, 3006 (1997).
[18] G. Q. Li and R. Machleidt, Phys. Rev. C **48**, 1702 (1993); **49**, 566 (1994).
[19] C. Fuchs, A. Faessler, and M. El-Shabshiry, Phys. Rev. C **64**, 024003 (2001).
[20] F. Sammarruca and P. Krastev, Phys. Rev. C **73**, 014001 (2006).
[21] V. R. Pandharipande and S. C. Pieper, Phys. Rev. C **45**, 791 (1992).
[22] K. A. Brueckner, S. A. Coon, and J. Dabrowski, Phys. Rev. **168**, 1184 (1968).
[23] I. Bombaci and U. Lombardo, Phys. Rev. C **44**, 1892 (1991).
[24] W. Zuo, I. Bombaci, and U. Lombardo, Phys. Rev. C **60**, 024605 (1999).
[25] I. Bombaci, T. T. S. Kuo, and U. Lombardo, Phys. Rep. **242**, 165 (1994).
[26] W. Zuo, Z. H. Li, A. Li, and G. C. Lu, Phys. Rev. C **69**, 064001 (2004).
[27] H. F. Zhang, Z. H. Li, U. Lombardo, P. Y. Luo, F. Sammarruca, and W. Zuo, Phys. Rev. C **76**, 054001 (2007).
[28] D. Alonso and F. Sammarruca, Phys. Rev. C **67**, 054301 (2003).
[29] F. Sammarruca, B. Chen, L. Coraggio, N. Itaco, and R. Machleidt, Phys. Rev. C **86**, 054317 (2012).
[30] F. Sammarruca, Eur. Phys. J. A **50**, 22 (2014).
[31] X. L. Shang, A. Li, Z. Q. Miao, G. F. Burgio, and H.-J. Schulze, Phys. Rev. C **101**, 065801 (2020).
[32] X.-L. Shang, J.-M. Dong, W. Zuo, P. Yin, and U. Lombardo, Phys. Rev. C **103**, 034316 (2021).
[33] G. C. Yong, Phys. Rev. C **96**, 044605 (2017).
[34] B. A. Li, L. W. Chen, and C. M. Ko, Phys. Rep. **464**, 113 (2008).
[35] B. A. Li and L. W. Chen, Phys. Rev. C **72**, 064611 (2005).
[36] W. M. Guo, G. C. Yong, Y. J. Wang, Q. F. Li, H. F. Zhang, and W. Zuo, Phys. Lett. B **726**, 211 (2013).
[37] W. M. Guo, G. C. Yong, and W. Zuo, Phys. Rev. C **90**, 044605 (2014).
[38] R. B. Wiringa, V. G. J. Stoks, and R. Schiavilla, Phys. Rev. C **51**, 38 (1995).
[39] P. Grangé, A. Lejeune, M. Martzolff, and J.-F. Mathiot, Phys. Rev. C **40**, 1040 (1989).
[40] Z. H. Li, U. Lombardo, H.-J. Schulze, and W. Zuo, Phys. Rev. C **77**, 034316 (2008); Z. H. Li and H.-J. Schulze, *ibid.* **78**, 028801 (2008).
[41] W. Zuo, A. Lejeune, U. Lombardo, and J.-F. Mathiot, Nucl. Phys. A **706**, 418 (2002); Eur. Phys. J. A **14**, 469 (2002).
[42] H. Q. Song, M. Baldo, G. Giansiracusa, and U. Lombardo, Phys. Rev. Lett. **81**, 1584 (1998).
[43] M. Schmidt, G. Röpke, and H. Schulz, Ann. Phys. **202**, 57 (1990).
[44] N. Kaiser, Eur. Phys. J. A **48**, 58 (2012).
[45] A. Dyhdalo, R. J. Furnstahl, K. Hebeler, and I. Tews, Phys. Rev. C **94**, 034001 (2016).
[46] M. F. Jiang and T. T. S. Kuo, Nucl. Phys. A **481**, 294 (1988).
[47] B. E. Vonderfecht, C. C. Gearhart, W. H. Dickhoff, A. Polls, and A. Ramos, Phys. Lett. B **253**, 1 (1991).
[48] T. Alm, G. Röpke, and M. Schmidt, Phys. Rev. C **50**, 31 (1994).
[49] X. L. Shang and W. Zuo, Phys. Rev. C **88**, 025806 (2013); X. L. Shang, P. Wang, P. Yin, and W. Zuo, J. Phys. G: Nucl. Part. Phys. **42**, 055105 (2015).
[50] X. H. Fan, X. L. Shang, J. M. Dong, and W. Zuo, Phys. Rev. C **99**, 065804 (2019).
[51] Q. F. Li, Z. X. Li, S. Soff, M. Bleicher, and H. Stöcker, J. Phys. G: Nucl. Part. Phys. **32**, 407 (2006).
[52] Q. F. Li, C. W. Shen, C. C. Guo, Y. J. Wang, Z. X. Li, J. Lukasik, and W. Trautmann, Phys. Rev. C **83**, 044617 (2011).
[53] Y. J. Wang, C. C. Guo, Q. F. Li, H. F. Zhang, Z. X. Li, and W. Trautmann, Phys. Rev. C **89**, 034606 (2014).
[54] A. Bol, P. Devescovi, P. Leleux, P. Lipnik, P. Macq, and J. P. Meulders, Phys. Rev. C **32**, 623 (1985).
[55] V. Grundies *et al.*, Phys. Lett. B **158**, 15 (1985).
[56] K. Chen *et al.*, Phys. Rev. **166**, 949 (1968).
[57] Y. X. Zhang, Z. X. Li, and P. Danielewicz, Phys. Rev. C **75**, 034615 (2007).